Beach vortices near circular topography

A. K. Hinds, E. R. Johnson, and N. R. McDonald

Citation: Physics of Fluids **28**, 106602 (2016); doi: 10.1063/1.4966038
View online: http://dx.doi.org/10.1063/1.4966038
View Table of Contents: http://scitation.aip.org/content/aip/journal/pof2/28/10?ver=pdfcov
Published by the AIP Publishing

PHYSICS OF FLUIDS **28**, 106602 (2016)

Beach vortices near circular topography

A. K. Hinds, E. R. Johnson, and N. R. McDonald
Department of Mathematics, University College London, Gower Street, London WC1E 6BT, United Kingdom

(Received 13 May 2016; accepted 11 October 2016; published online 31 October 2016)

Finite-area monopolar vortices which propagate around topography without change in shape are computed for circular seamounts and wells including the limiting cases of each: islands and infinitely deep wells. The time-dependent behaviour of vortex pairs propagating toward circular topography is also examined. Trajectories of point-vortex pairs exterior to the topography are found and compared to trajectories of vortex patches computed using contour dynamics.
[http://dx.doi.org/10.1063/1.4966038]

I. INTRODUCTION

Geophysical vortices ranging in size from surf-zone vortices to large-scale ocean eddies are notable for their long lifetimes. It is thus likely that these vortices will encounter topographic obstacles: observations in the Canary Basin[1] have shown meddies (Mediterranean salt lenses) interacting strongly with seamounts in the North Atlantic, and North Brazil Current Rings hundreds of kilometres in diameter have been observed[2] colliding with islands in the Caribbean. It has also been shown[3] that vortices frequently "pair up" in the surf zone to form finite-area vortex pairs which survive for several eddy-turnover periods[4] and so, again, are likely to encounter topographic obstacles. Computations for an initially distant Lamb dipole approaching a circular cylinder head-on show that the dipole splits and passes around the cylinder before pairing up on the far side and propagating away from the cylinder.[5] Laboratory experiments[6] found that the cylinder diameter affects the vortex trajectories significantly. These observations motivated a study[7] of point vortex and vortex-patch motion around two impermeable circular cylinders where the point-vortex motion is shown to be governed by a Hamiltonian, derivable from complex variable techniques which extend directly[8] to point-vortex motion around multiple cylinders.

Dipolar[9,10] and monopolar[11] surf-zone vortices (i.e., zero background rotation) have been studied analytically near a step of finite depth-ratio. The analytic expression of the Green's function for a point vortex near stepped topography showed that a point vortex is unable to cross the step as its velocity parallel to the step becomes unbounded as it approaches the step. In contrast, numerical computations for dipolar (i.e., equal and oppositely signed) vortex patches colliding head-on with the step showed that patches are able to cross the step,[9] and the patches either move closer to each other and accelerate or move apart and decelerate according to whether they approach from deep or shallow water.

In addition to these collision studies, it is of interest to consider distributions of vorticity that evolve without change of form. In the absence of topography, the calculation of two-dimensional distributions of patches of constant vorticity governed by the Euler equations in steady translation or rotation, the so-called V-states, is well established.[12–15] Typically, translating V-states consist of a pair of symmetric but oppositely signed patches of vorticity,[12,13] so the velocity normal to the symmetry axis vanishes, and the axis may be replaced by an impermeable wall.[14] Monopolar V-states propagating parallel to a step change in depth have also been found.[11] V-states lying entirely in deep water resemble vortex patches near a wall,[13,14,16] while V-states lying entirely in shallow water resemble an individual vortex from a co-rotating pair of same-signed vortices.[15] V-states straddling the escarpment combine these forms. Integrations in time-dependent codes showed that the V-states

were robust and acted as attractors in that initially circular straddling patches shed vorticity to approach shapes close to those of a V-state.

The aim of the present work is to present similar results for beach vortices near finite-height circular topography: investigating the properties of steady state monopolar patches and time-dependent scattering of dipolar vortex structures to demonstrate the far richer range of behaviours possible when the topographic perturbation is of finite extent.

Finite-area monopolar V-states orbiting circular topography are computed, including the limiting case where the cylinder passes through the whole of the fluid depth (island) or when a vortex is trapped with in a circular domain (deep well). The problem is tackled by finding the appropriate Green's function (Section III) from the conservation of vorticity with pressure and normal mass flux continuous across the topographic boundary. Unlike previous studies[7] in which the streamfunction was found by first ignoring the boundaries and then evaluating a complementary irrotational flow so the normal velocity of the combined flow is zero at the boundaries, a different method, avoiding these supplementary computations, is introduced. Section IV describes the form of the steadily propagating solutions and their robustness is tested using time-dependent contour dynamics. Section V determines the trajectories of a point-vortex pair (having equal and opposite circulation) close to finite-height circular topography explicitly using Hamiltonian techniques. It is found that trajectories of a vortex pair near circular topography can be classified into three different classes: (i) both vortices exist exterior to the topography, (ii) both vortices exist interior to the topography, and (iii) one vortex is interior where the other is exterior to the topography. Trajectories in which a distant point-vortex pair approaches the topography are considered with seamounts and wells discussed separately. It is found that the resulting trajectories can be divided into four classes: (i) an approaching pair bifurcates with each vortex in the pair passing on opposite sides of the topography, (ii) an approaching pair does not bifurcate and passes the same side of the topography, (iii) each vortex is trapped in orbits about the topography with different frequencies, and (iv) an equilibrium state where each vortex is trapped by the topography, having identical rotation frequencies. Section V also follows the evolution of vortex-patch pairs using contour dynamics, comparing trajectories with point-vortex-pair trajectories. Section VI draws some conclusions.

II. GOVERNING EQUATIONS

The two-dimensional flow of a shallow, homogeneous inviscid fluid bounded below by finite-height bottom topography and above by a horizontal rigid lid is governed by the conservation of potential vorticity,

$$q_t + \mathbf{u} \cdot \nabla q = 0, \tag{1}$$

where $q = \omega/H$, H is the fluid depth, $\omega = v_x - u_y$ the vertical component of the vorticity, and (u, v) the horizontal components of the velocity. Conservation of mass, $\nabla \cdot (H\mathbf{u}) = 0$, allows a streamfunction ψ to be introduced as

$$(u, v) = H^{-1}(\psi_y, -\psi_x). \tag{2}$$

Provided the vorticity decays sufficiently rapidly with distance to give convergent integrals, the circulation, Γ, and kinetic energy, $\mathcal{E}$,

$$\Gamma = \int \omega \, \mathrm{d}x \, \mathrm{d}y, \qquad \mathcal{E} = \int \psi\omega \, \mathrm{d}x \, \mathrm{d}y, \tag{3}$$

are invariants above arbitrary topography.[11] For topography that varies in the radial direction only, the angular impulse $\mathcal{J}$ can be shown to be a third constant of motion[11] where

$$\mathcal{J} = \int R\omega r \, \mathrm{d}r \, \mathrm{d}\theta, \qquad \text{for} \qquad R(r) = \int^r H(r')r' \, \mathrm{d}r'. \tag{4}$$

For topography consisting of a single step at $r = 1$ between flat regions of depth H^- in $r < 1$ and depth H^+ in $r > 1$, R can be taken to be

$$R(r) = \begin{cases} \frac{1}{2}H^- r^2 & \text{if } r \le 1, \\ \frac{1}{2}H^+(r^2-1) + \frac{1}{2}H^- & \text{if } r > 1. \end{cases} \tag{5}$$

Since R is a monotonically increasing function of r, a centre of vorticity (r_c, θ_c) can be associated with any bounded vorticity distribution ω where

$$R(r_c) = \mathcal{J}/\Gamma, \qquad \theta_c = \int \theta\omega r \, \mathrm{d}r \, \mathrm{d}\theta/\Gamma, \tag{6}$$

with r_c, found by inverting (5), lying within the r-extremes of the vorticity distribution and θ_c the standard θ-mean. The point vortex equivalent to a given vortex patch above axisymmetric topography can thus be defined as the point vortex with the same circulation and same centre of vorticity as the patch.

III. THE GREEN'S FUNCTION

Contour dynamics has been highly successful in investigating the evolution of piecewise-constant vorticity. Several studies[7,17,18] have incorporated specific, non-trivial boundaries by first ignoring boundaries and using contour dynamics to find the velocity field due to vortices alone and then computing (typically through conformal mapping) an irrotational flow field that cancels the flow normal to the boundaries. The two fields superpose to give the unique total velocity for advancing the flow. The alternative approach[19] presented here avoids the supplementary computations by modifying the Green's function in the contour dynamics integrations (as has been done for channel flow[20] and geometries that can be conformally mapped to a simpler circular domain[21]). This method applies to circular topography with finite depth changes and also extends to free-surface flows where the governing equation is the inhomogeneous Helmholtz equation instead of the Poisson's equation considered here.

Contours separating regions of constant potential vorticity are advected according to (1) by the velocity field (2) which is determined from the instantaneous vertical component of vorticity by inverting

$$\omega = v_x - u_y = -\nabla \cdot (H^{-1}\nabla\psi) \tag{7}$$

for the streamfunction ψ. Since (7) is linear in ψ the inversion for multiple patches of constant, but perhaps differing, vorticities follow as a linear combination of the solutions for the individual patches. It is thus sufficient to consider a single region $\mathcal{R}$ of constant unit vorticity for which the inversion can be written in terms of a Green's function G in the form

$$\psi(x,y) = \iint_{\mathcal{R}} G(x,y,x_0,y_0)\,\mathrm{d}x_0\,\mathrm{d}y_0. \tag{8}$$

It is convenient in the manipulations below, and computationally, to introduce the depth-integrated, or transport, velocity components $(U,V) = (Hu, Hv)$ which, from (8) and (2), can be written

$$U + \mathrm{i}V = \frac{\partial\psi}{\partial y} - \mathrm{i}\frac{\partial\psi}{\partial x} = \iint_{\mathcal{R}} \left(\frac{\partial G}{\partial y} - \mathrm{i}\frac{\partial G}{\partial x}\right) \mathrm{d}x_0\,\mathrm{d}y_0. \tag{9}$$

Now suppose that the (x,y)-partial derivatives of $G(x,y,x_0,y_0)$ are related to the (x_0,y_0)-partial derivatives of some function $\hat{G}(x,y,x_0,y_0)$ through

$$\frac{\partial G}{\partial x} = g_{11}(x,y)\frac{\partial \hat{G}}{\partial x_0} + g_{12}(x,y)\frac{\partial \hat{G}}{\partial y_0}, \qquad \frac{\partial G}{\partial y} = g_{21}(x,y)\frac{\partial \hat{G}}{\partial x_0} + g_{22}(x,y)\frac{\partial \hat{G}}{\partial y_0}. \tag{10}$$

Then substituting (10) in (9) and using Green's theorem to replace the integral over the (x_0,y_0)-region $\mathcal{R}$ by the line integral taken anticlockwise around its closed boundary $\partial\mathcal{R}$ gives

$$U + \mathrm{i}V = -(g_{22} - \mathrm{i}g_{12}) \oint_{\partial\mathcal{R}} \hat{G}\,\mathrm{d}x_0 + (g_{21} - \mathrm{i}g_{11}) \oint_{\partial\mathcal{R}} \hat{G}\,\mathrm{d}y_0. \tag{11}$$

For the special case when G depends on the distance $|z - z_0|$ alone (where $z = x + \mathrm{i}y$ and $z_0 = x_0 + \mathrm{i}y_0$), $\hat{G}$ can be identified with G so $g_{11} = -1$, $g_{12} = 0$, $g_{21} = 0$, $g_{22} = -1$, and (11) reduces to the usual unbounded-domain expression,

$$U + \mathrm{i}V = \oint_{\partial\mathcal{R}} G \, \mathrm{d}z_0, \tag{12}$$

as in Ref. 22, once the sign errors there in Equations (2) and (4) on page 164 are corrected.

A useful application of (11) follows for a Green's function where boundary effects can be represented by a finite system of image vortices. Let a vortex at z_0 has N images $Z_k(z_0) = X_k(z_0) + \mathrm{i}Y_k(z_0)$, $k = 1, \ldots, N$. Thus the Green's function has the form

$$G(x, y, x_0, y_0) = \sum G_k(|z - Z_k(z_0)|^2), \tag{13}$$

where the sum is taken over $k = 0, \ldots, N$ with $Z_0(z_0) = z_0$, the identity, corresponding to the vortex itself. The Green's function depends solely on the distances from the observation point z to the vortex and its images. By symmetry between the reference point z_0 and the observation point z of the Green's function, it follows that

$$G(x, y, x_0, y_0) = G(x_0, y_0, x, y) = \sum G_k(|z_0 - Z_k(z)|^2). \tag{14}$$

Differentiating (14) with respect to x gives

$$\begin{aligned}
&\frac{\partial G}{\partial x}(x, y, x_0, y_0) \\
&\quad = -2 \sum G_k'(|z_0 - Z_k(z)|^2) \left\{ [x_0 - X_k(x, y)] \frac{\partial X_k}{\partial x} + [y_0 - Y_k(x, y)] \frac{\partial Y_k}{\partial x} \right\} \\
&\quad = - \sum \left\{ \frac{\partial G_k}{\partial x_0}(|z_0 - Z_k(z)|^2) \frac{\partial X_k}{\partial x}(x, y) + \frac{\partial G_k}{\partial y_0}(|z_0 - Z_k(z)|^2) \frac{\partial Y_k}{\partial x}(x, y) \right\},
\end{aligned} \tag{15}$$

and, analogously, $\partial G / \partial y$. These are of form (10) and so (11) gives

$$U + \mathrm{i}V = \mathrm{i} \sum \left\{ \left(\frac{\partial Y_k}{\partial x} + \mathrm{i} \frac{\partial Y_k}{\partial y} \right) U_k - \left(\frac{\partial X_k}{\partial x} + \mathrm{i} \frac{\partial X_k}{\partial y} \right) V_k \right\}, \tag{16}$$

where

$$U_k + \mathrm{i}V_k = \oint_{\partial\mathcal{R}} G_k(|z_0 - Z_k(z)|^2) \, \mathrm{d}z_0 \tag{17}$$

is the depth-integrated velocity induced at the kth image $Z_k(z)$ of the observation point z. The velocity at the observation point z is simply the sum of multiples of the velocity induced at the N image points of z which follow from integrating the Green's functions G_k around $\partial\mathcal{R}$, the boundary of the original vortex, alone. This is particularly efficient when using contour dynamics since no additional calculations are required to determine boundary effects. When the images are absent (16) reduces to (12) as expected. The normal component of velocity is discontinuous across the escarpment, being greater on the shallow side corresponding to the generation of area to conserve volume. In the time-dependent computations reported below no discernible changes were observed between taking a point lying instantaneously precisely on the escarpment as being in shallow or deep water, probably because no such precise equality occurred.

For the circular step topography, requiring the mass flux and pressure to be continuous across the step[10] gives the Green's function[23]

$$G(z, z_0) = -\frac{1}{2\pi} \begin{cases} H^+[\log|z - z_0| + \alpha \log|1 - 1/(z\bar{z}_0)|], & |z| > 1, |z_0| > 1, \\ H^+[\beta \log|z - z_0| - \alpha \log|z_0|], & |z| < 1, |z_0| > 1, \\ H^+[\beta \log|z - z_0| - \alpha \log|z|], & |z| > 1, |z_0| < 1, \\ H^-[\log|z - z_0| - \alpha \log|1 - z\bar{z}_0|], & |z| < 1, |z_0| < 1, \end{cases} \tag{18}$$

where $\bar{z}$ is the conjugate of z,

$$\alpha = (\gamma - 1)/(\gamma + 1), \qquad \beta = 1 + \alpha, \quad \text{and} \quad \gamma = H^-/H^+, \tag{19}$$

the depth ratio. The Green's function G is continuous at $|z| = 1$ and symmetric in z and z_0, as required. Moreover in the neighbourhood of the vortex at z_0,

$$G(z, z_0) \to -\frac{H(z_0)}{2\pi} \log|z - z_0|, \quad \text{as } z \to z_0, \tag{20}$$

as required. When $|z|, |z_0| < 1$, expression (18) gives two singularities of equal and opposite strength at $z = 0$. Appendix A gives an alternative formulation, valid for all $|z|, |z_0| < 1$, but particularly accurate near the origin.

Now G is of form (13) with $Z_1(z) = 1/\bar{z}$ so the complex velocity, using (16), is (taking $\omega(x_0, y_0) = 1$)

$$u + \mathrm{i}v = \frac{1}{2\pi} \begin{cases} H^+[(u_0 + \mathrm{i}v_0) + \alpha(u_1 - \mathrm{i}v_1)/\bar{z}^2], & |z| > 1, |z_0| > 1, \\ H^+\beta(u_0 + \mathrm{i}v_0), & |z| < 1, |z_0| > 1, \\ H^+[\beta(u_0 + \mathrm{i}v_0) - \mathrm{i}\alpha H^+ \mathcal{A}/\bar{z}], & |z| > 1, |z_0| < 1, \\ H^-[(u_0 + \mathrm{i}v_0) - \alpha(u_1 - \mathrm{i}v_1)/\bar{z}^2 - \mathrm{i}\alpha\mathcal{A}/\bar{z}], & |z| < 1, |z_0| < 1, \end{cases} \tag{21}$$

where $\mathcal{A}$ is the area of the patch in $|z_0| < 1$ and the subscripts 0, 1 represent contributions from the vortex and the effects of the topography, respectively. The formulation here modifies the usual discussions in terms of images. The standard way to find the velocity of a point vortex in relatively deep water outside the topography ($\gamma < 1$ and $r_0 > 1$) is to consider two image vortices of strength α—one at $z = 1/\bar{z}_0$ with oppositely signed circulation and one at the origin with same-signed circulation.[24] In the method here the same point is advected by a single image point vortex at $z = 1/\bar{z}_0$ with strength, from (21), modified by a factor $1/\bar{z}^2$. The flow inside the cylinder is driven by a vortex outside the cylinder modified by the factor β. A vortex inside the cylinder, in relatively shallow water, is advected by an image at $z = 1/\bar{z}_0$ with strength $-\alpha$ and an image at the origin with strength $-\alpha$. Flow outside the cylinder when the vortex is inside the cylinder is driven by the vortex with strength β and an image vortex of strength $-\alpha$. The image strength α and the residual vortex strength β have ranges $-1 < \alpha < 1$, $0 < \beta < 2$ with the extreme values corresponding to a circular wall ($\gamma = 0$) and an infinitely deep well ($\gamma \to \infty$), respectively. Figure 1 gives contours of G and so point-vortex volume-flux streamlines for a high seamount ($\gamma = 0.1$) and a deep well ($\gamma = 10$). In the absence of topography ($\gamma = 1$), the streamlines are smooth and given by (20) everywhere. In the limits $\gamma \to 0$ and $\gamma \to \infty$, when the topography occupies the whole depth and the cylinder is impermeable, the limiting case for (a) is a point vortex outside a cylinder with zero circulation about the cylinder, for (b), flow outside a cylinder with fixed circulation about the cylinder, for (c), a stagnant well, and for (d), a point vortex inside an impenetrable well.

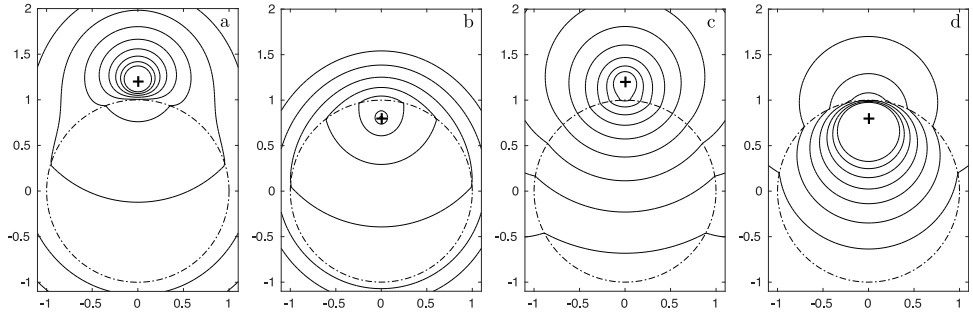

FIG. 1. Equally spaced contours of the Green's function (18), and thus streamlines for the point-vortex volume-flux streamfunction. The escarpment edge is dashed-dotted and + marks the vortex centre, z_0. Flow is anti-clockwise around the streamlines for positive vortices. In (a) ($z_0 = 1.2\mathrm{i}$) and (b) ($z_0 = 0.8\mathrm{i}$), $\gamma = 0.1$, giving a high seamount with little flow over the seamount. In (c) ($z_0 = 1.2\mathrm{i}$) and (d) ($z_0 = 0.8\mathrm{i}$), $\gamma = 10$, giving a deep well.

IV. MONOPOLAR VORTICES TRAPPED BY FINITE-HEIGHT CIRCULAR TOPOGRAPHY

A. Equilibrium states for vortex patches trapped around circular topography

Finite-area vortices which rotate around the circular topography at constant angular velocity without change in form (equilibrium states or V-states) can be constructed numerically using an algorithm which ensures the vortex boundary is a streamline. The necessary velocity field along the vortex boundary is computed using contour dynamics with the Green's function (18). Details of the algorithm are given in Appendix B and closely follow the previous work.[14] That is, starting with an initially circular contour, velocity components are computed at $N+1$ nodes along the vortex boundary using contour dynamics. The nodal positions are then adjusted iteratively so that the boundary is parallel to the local velocity by satisfying a $(N+1)\times(N+1)$ tri-diagonal system of algebraic equations at each iteration. This iterative process of using contour dynamics to find the velocity at each node and then adjusting the boundary by solving the tri-diagonal system of equations is repeated until a tolerance, $\epsilon = 10^{-8}$, for the steady angular velocity, Ω, is met. Typically this is achieved in 50–60 iterations, using a resolution of 4704 nodes around an initially circular patch of unit radius. For vortices straddling the topography, contributions to the velocity field owing to vorticity distributions on each side of the step are computed separately.

B. V-states near finite-height topography

Figure 2 gives examples of V-states near finite-height circular topography with unit radius for two examples of the depth ratio. Each subframe corresponds to a fixed value of the centre of vorticity r_c and shows V-states with areas increasing from one tenth to four times the cylinder area. The shape of V-states can be predicted using a self-gravitating body analogy.[23] V-states close but exterior a cylinder in deep water are repelled by their image, with the side closest to the escarpment stretching around the topography. With the depth ratio inverted, $\gamma > 1$ so the V-state is in relatively shallow water, the vortex is attracted by its image with V-states appearing tear-like. Figure 2(a) shows V-states near a seamount with $\gamma = 1/2$. V-states with centroids near the centre of the topography have near circular shape since the contributions from images points are close to symmetric. Small (in comparison to the radius of the topography) V-states which exist wholly outside or inside but close to the step have similar shapes to V-states near finite-height rectilinear topography.[11] In general straddling V-states have distorted shapes, whereas sufficiently large enveloping V-states (where the whole seamount lies inside the vortex) deviate only a small amount from circular. Figure 2(b) gives V-states near a well with $\gamma = 2$. Vortices outside the well are stretched toward the topography and vortices inside the well flatten along the edge of the topography.

Figure 3 compares the orbital angular velocity (plotted as a function of r_c) of a V-state with a point vortex having equivalent circulation (normalized to π) and centre of vorticity for two values of depth ratio; (a) $\gamma = 1/2$, (b) $\gamma = 2$. Each curve in each frame represents a different choice of patch volume. As expected the angular orbital velocity of small vortex patches agrees well with that of a point vortex. This is particularly true at large distances where the patch is close to circular. The orbital velocity of larger patches near topography deviates more as these V-states are no longer near circular. For patch volume π and $\gamma = 1/2$, the patch lies over the step and can no longer be simply modelled as a point vortex.

C. Limiting cases for finite-height circular topography

In the limit $\gamma \to 0$, a rectilinear escarpment becomes a rigid wall occupying the entire fluid depth and the vortex propagates along it.[12–14,16] For finite-height circular topography, there are two limiting cases for vortex motion: first, when the vortex translates exterior to a circular island and second, when the vortex is trapped inside a circular well. The Green's function for each case is given by (18) with $\alpha = \pm 1$, simplified by noting that there is no contribution from terms involving $|z| < 1, |z_0| > 1$ and $|z| > 1, |z_0| < 1$.

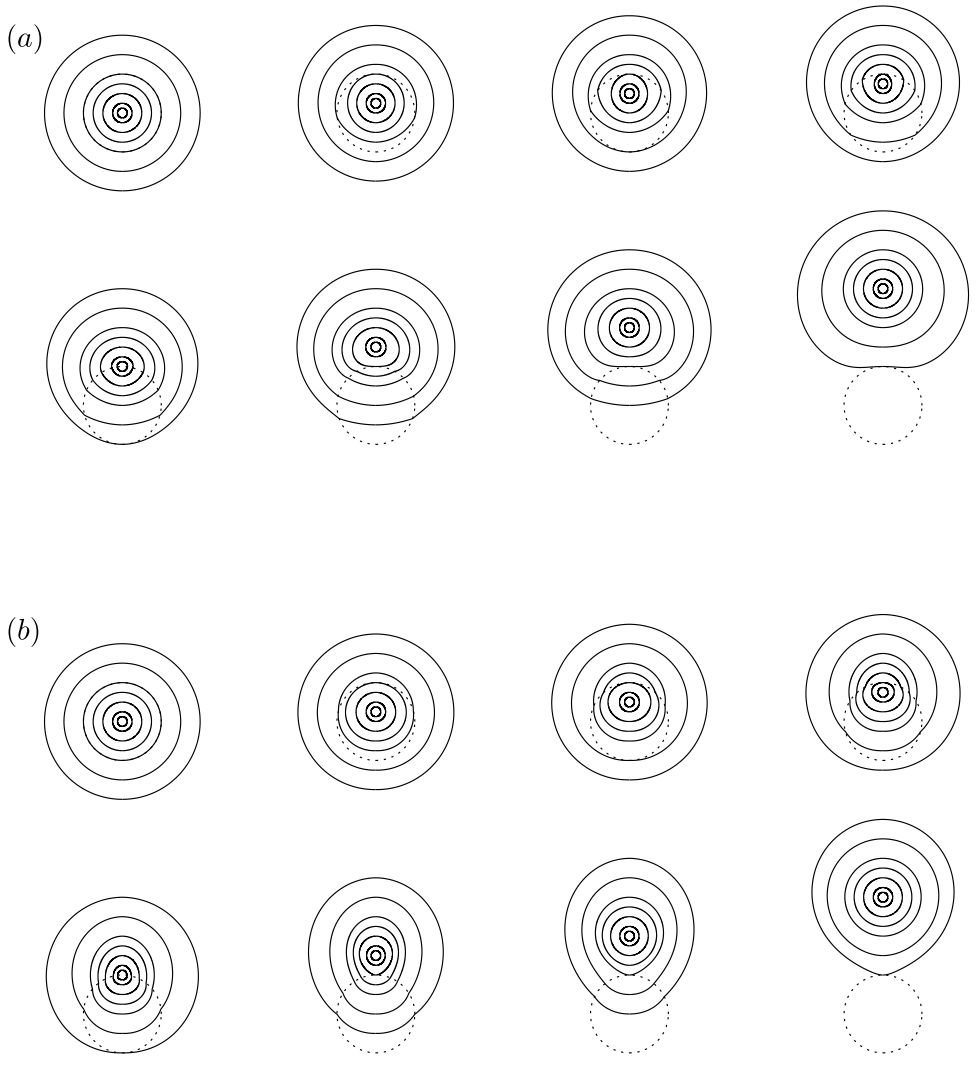

FIG. 2. V-states near finite-height topography. (a) Depth ratio $\gamma = 1/2$ so deep water lies outside the cylinder and (b) $\gamma = 2$ with deep water inside the cylinder. Each frame shows seven V-states with collated vortices in each frame having mean radii $\frac{1}{8}$, $\frac{1}{4}$, $\frac{1}{2}$, $\frac{3}{4}$, 1, 2, 3 with the cylinder having radius 1. The dotted line gives the location of the finite-height topography.

Figure 4(a) gives examples of V-states trapped inside a well of unit radius, and Figure 4(b) gives V-states outside an island. Shapes of V-states in both cases may be anticipated from extreme cases of finite-height topography: small vortices (compared to the cylinder radius) exterior or interior to the cylindrical wall near the solid boundary resemble V-states near a rectilinear wall.[12–14,16] Whereas V-states far from the boundary interact weakly with the topography and remain close to circular.

Figure 5 gives the angular velocity of the disjoint exterior V-states and the interior V-states as a function of r_c in these limiting cases for two patch volumes, with the angular speed for a point vortex with the same centre of vorticity and circulation included for comparison. There is good agreement between computed V-state speeds and point vortex speeds where comparison is possible. The V-state plots terminate when the patch touches the boundary of the topography as no V-states of these areas exist beyond this value of r_c. The angular velocity of the V-states starts to deviate from the point vortex approximation when V-states approach the boundary and distort. The point vortex approximation applies without modification to the enveloping exterior V-states and the agreement with computed speeds is equally close.

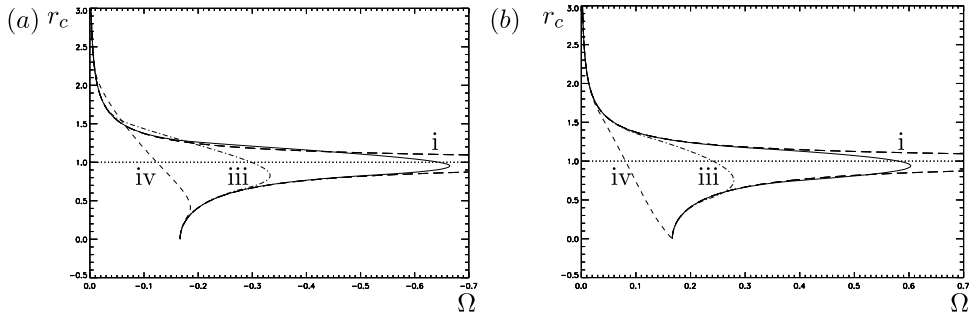

FIG. 3. The V-state angular velocity Ω as a function of the centre of vorticity r_c for (a) $\gamma = 1/2$ and (b) $\gamma = 2$ for vortex patches of circulation π. The long dashes (i) show an equivalent point vortex both interior and exterior to the topography whose boundary is given by the dotted line, $r_c = 1$, corresponding to the unit radius topography of Figure 2. The solid line shows the velocity of a patch with volume $\pi/16$, the dashed-dotted line (iii) for volume $\pi/4$ and shorter dashes (iv) for volume π.

D. V-states in time-dependent flows

1. Using a computed V-state to initialize the flow

To investigate the robustness (i.e., the finite-amplitude stability) of these computed V-states, the time-dependent equations of motion, initialized with a computed V-state, were integrated using a fourth-order Runge-Kutta scheme and contour surgery.[25] Figure 6 gives two examples of these integrations: Figure 6(a) ($\gamma = 1/2$) shows the vortex patch after 25 eddy-turnover times (more than two orbits of the topography) with the initial computed V-state for comparison; Figure 6(b) shows the equivalent case for $\gamma = 2$. The evolved vortex patches compare favourably to the original V-states, suggesting that they are highly durable, stable structures. There is a little vortex shedding during the integrations caused by the finite resolution of the time-dependent numerical algorithm[25] and the removal of tiny filaments generated during the motion also causes the centre of vorticity to be displaced slightly. Both of these effects are remarkably small given the significant extent (in space and time) of the integration.

2. Using a circular patch to initialize the flow

In addition to the apparent stability of V-states, it is of interest to determine whether arbitrarily shaped patches can evolve towards equilibrium states: do V-states act as attractors for the flow? To address this question time-dependent integrations were performed using an initially circular vortex patch. The general conclusion is that since the initial state is not precisely a V-state it must shed vorticity (when contour surgery is allowed, or generate infinitely long, arbitrarily thin filaments in the absence of surgery) to approach a V-state. If this is possible without the patch disintegrating entirely then the V-state is indeed an attractor. Integrations (not shown here) where the initial patch does not straddle the topography do not shed vorticity but instead circle the topography, conserving energy and angular impulse, with shape oscillating about that of a V-state as observed previously exterior to cylindrical islands.[7] Patches initially straddling the escarpment shed vorticity, changing their energy and impulse as in Figure 7 which shows eight snapshots of the evolving flow for two cases: (a) $\gamma = 1/5$ and (b) $\gamma = 3$. The final frame in each series shows the closeness of the evolved patch at time $t = 14$ (starred to denote the rotated presentation) to the V-state with the same circulation and centre of vorticity as the evolved patch. Although vortex shedding is necessary for a non-V-state patch to approach a V-state, too much shedding causes the patch to evolve to be very different from its initial form. Figure 8 contrasts the evolution of two identical patches, both larger than those of Figure 7, with different depth ratios, $\gamma = 3$ and $\gamma = 2$. The larger contrast in depth causes the patch to shed severely, whereas over the smaller depth contrast the patch sheds only sufficient vorticity to approach a nearby V-state. The magnitude of the deviation of the initial condition from the V-state also affects breakup. The topography in Figures 7(b) and 8(a) is the same but the larger patch of Figure 8(a) deviates more from nearby V-states than the smaller patch of Figure 7(b) leading to the larger patch's breaking up whereas the smaller patch retains most of its initial volume.

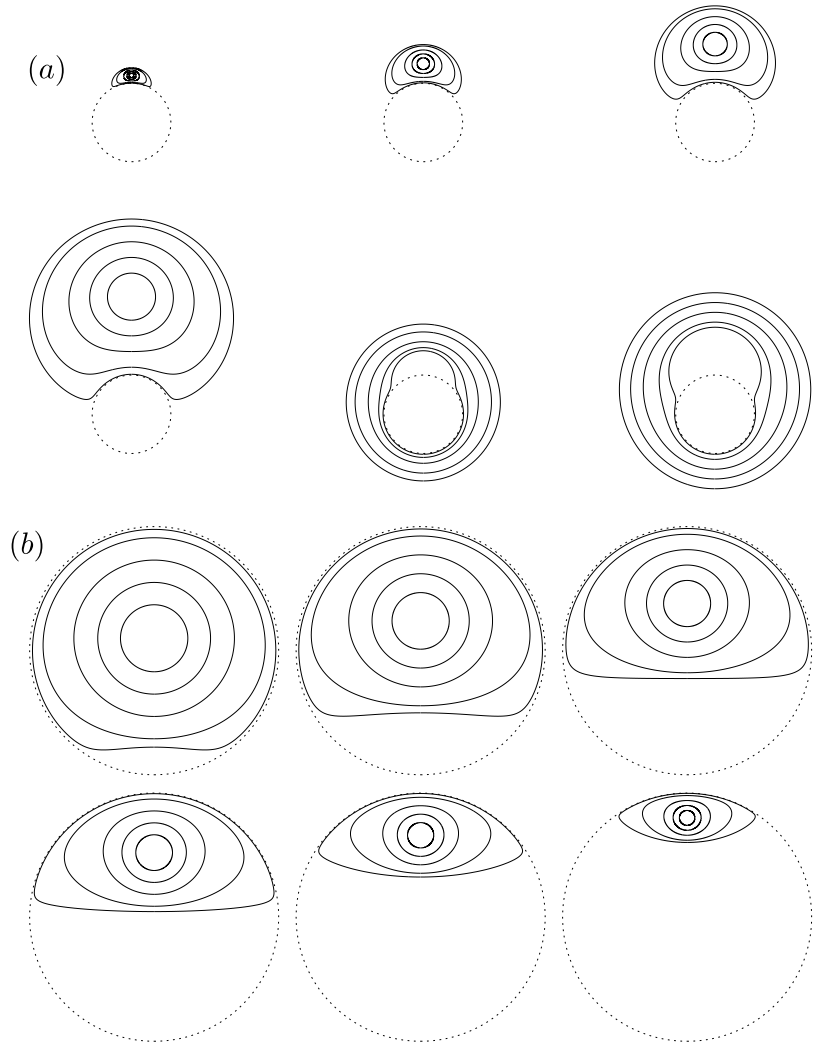

FIG. 4. V-states for topography that occupies the entire fluid depth. Each frame corresponds to a fixed value of the centre of vorticity, r_c. Within each frame V-states of differing areas illustrate the range from near-circular V-states to the most distorted shape of the limiting V-state touching the topography. (a) $\gamma = 0$: the cylinder occupies the entire depth. Here there are two possibilities: the V-state lies outside and is disjoint from the island, as in the first four frames, or the V-state envelops the island as in the final two frames. (b) $\gamma \to \infty$: the V-state is trapped within the well.

V. VORTEX PAIRS ENCOUNTERING CIRCULAR TOPOGRAPHY

A. Equations and the Hamiltonian structure for point vortex pairs

Section IV concentrates on single vortices trapped by topography. Another ubiquitous long-lived motion[26] is that of propagating vortex pairs. This section thus considers initially distant vortex pairs which, through mutual advection, approach circular topography. Attention is confined to a vortex pair of equal and oppositely signed circulation with each vortex centred at (r_1, θ_1) and (r_2, θ_2). Point-vortex trajectories can be found from the Kirchoff-Routh path function[22] or vortex Hamiltonian (without background flow) given by

$$\mathcal{H}(z_1, \ldots, z_N) = \frac{1}{2} \sum_{j=1}^{N} \sum_{k=j+1}^{N} Q_j H_j Q_k H_k G(z_j, z_k) + \frac{1}{2} \sum_{j=1}^{N} Q_j^2 H_j^2 g(z_j, z_j), \tag{22}$$

where $H_j = H(z_j)$ is the fluid depth at z_j and $g(z, z_j) = G(z, z_j) + 1/2\pi \log|z - z_j|$. As in the case of rectilinear topography,[11] a point vortex cannot cross the circular step (since its velocity parallel

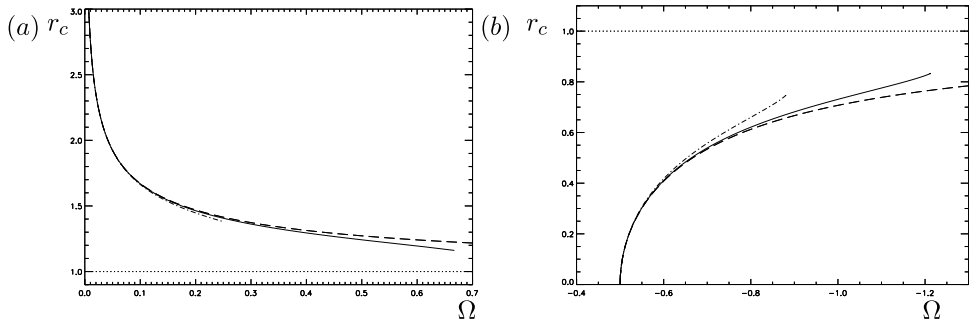

FIG. 5. The angular velocity Ω as a function of centre of vorticity r_c for topography that occupies the entire fluid depth for vortex patches of circulation π as in Figure 3: (a) exterior to the cylinder. (b) Interior to the cylinder. The long dashes correspond to the equivalent point vortex both interior and exterior to the topography whose boundary is again given by the dotted line. A solid line shows the velocity of a patch with volume $\pi/16$, dashed-dotted line shows V-states with volume $\pi/8$. The lines terminate when the patch touches the boundary of the topography.

to the step increases without limit as its displacement from the step decreases) and so point-vortex trajectories divide into three disjoint regimes: both vortices external to the cylinder ($r_1, r_2 > 1$), both interior ($r_1, r_2 < 1$), and one interior and one external ($r_2 < 1 < r_1$), giving the Hamiltonian

$$\mathcal{H} = \begin{cases} -\dfrac{H^+}{4\pi}\left\{\Gamma_1\Gamma_2 \log[r_1^2 + r_2^2 - 2r_1r_2\cos(\theta_1-\theta_2)] + \Gamma_1\Gamma_2\alpha \log\left[\dfrac{r_1^2r_2^2 - 2r_1r_2\cos(\theta_1-\theta_2)+1}{r_1^2r_2^2}\right]\right. \\ \qquad \left. + \Gamma_1^2\alpha \log\left[1-\dfrac{1}{r_1^2}\right] + \Gamma_2^2\alpha \log\left[1-\dfrac{1}{r_2^2}\right]\right\} \qquad (r_1, r_2 > 1) \\ -\dfrac{H^+}{4\pi}\left\{\Gamma_1\Gamma_2\beta \log[r_1^2 + r_2^2 - 2r_1r_2\cos(\theta_1-\theta_2)] - \Gamma_1\Gamma_2\alpha \log[r_1]\right. \\ \qquad \left. - \Gamma_1^2\alpha \log\left[1-\dfrac{1}{r_1^2}\right] + \gamma\Gamma_2^2\alpha \log[1-r_2^2]\right\} \qquad (r_2 < 1 < r_1) \\ -\dfrac{\gamma H^+}{4\pi}\left\{\Gamma_1\Gamma_2 \log[r_1^2 + r_2^2 - 2r_1r_2\cos(\theta_1-\theta_2)] - \Gamma_1\Gamma_2\alpha \log\left[\dfrac{r_1^2r_2^2 - 2r_1r_2\cos(\theta_1-\theta_2)+1}{r_1^2r_2^2}\right]\right. \\ \qquad \left. - \Gamma_1^2\alpha \log[1-r_1^2] - \Gamma_2^2\alpha \log[1-r_2^2]\right\} \qquad (r_1, r_2 < 1) \end{cases} \tag{23}$$

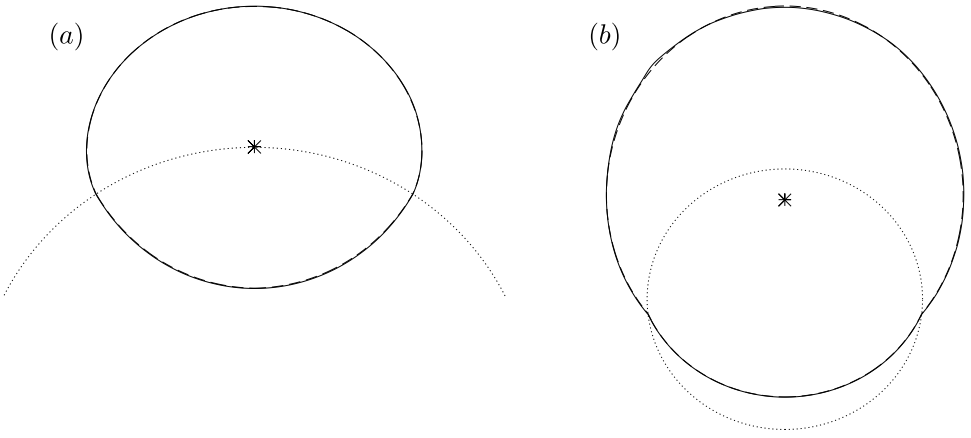

FIG. 6. Comparison between the initial and final states of a vortex patch starting from a computed V-state, (a) $\gamma = 1/2$ and (b) $\gamma = 2$. The dashed line gives the initial V-state (with the centre of vorticity marked by +) with the solid line the patch after 25 eddy-turnover times (with the centre of vorticity marked by ×). The dotted line here represents the topographic boundary for the circular topography.

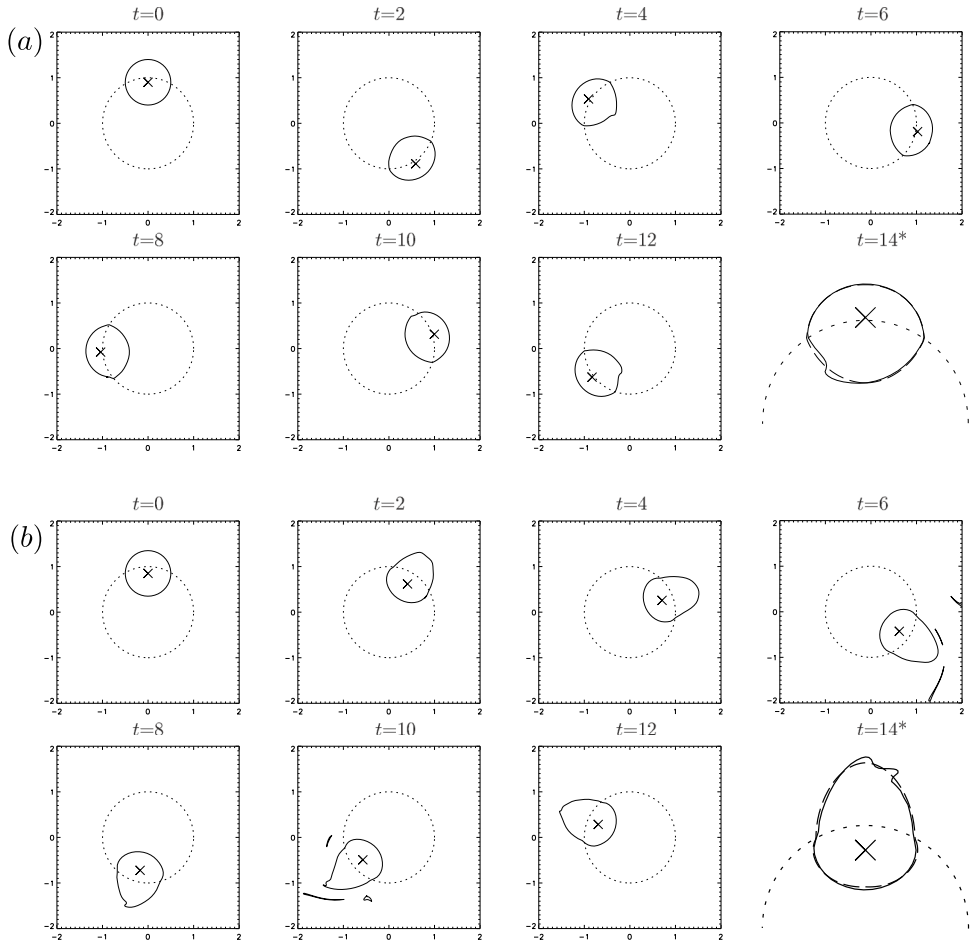

FIG. 7. The evolution of a vortex that is initially circular and straddling the topography for (a) $\gamma = 1/5$ and (b) $\gamma = 3$. Frames are shown at equal intervals, with the final frame ($t = 14$) in each series rotated, for clarity, so that the centre of vorticity lies on $x = 0$, i.e., $\theta_c = 0$. The final frames compare the evolved patch with the V-state, denoted by a long-dashed line, that has the same circulation and centre of vorticity as the evolved patch, with the semi-circular section of the escarpment shown by short dashes.

B. Trajectories of point-vortex pairs exterior to topography

Motivated by observations[1] and computations[27] where vortices encounter circular topography and occasionally bifurcate this section describes the trajectories of vortex pairs outside finite-height circular topography for a seamount, $\gamma < 1$, and a well, $\gamma > 1$, including the limiting cases of a surface piercing island $\gamma = 0$ and a deep well $\gamma \to \infty$. Write $\Gamma = \Gamma_1 = -\Gamma_2$, so (23) becomes

$$\mathcal{H}_{ext,ext} = \frac{\Gamma^2 H^+}{4\pi} \log\left[\frac{(r_1^2 + r_2^2 - 2r_1 r_2 \cos\phi)(r_1^2 r_2^2 - 2r_1 r_2 \cos\phi + 1)^\alpha}{(r_1^2 - 1)^\alpha (r_2^2 - 1)^\alpha}\right]. \tag{24}$$

The trajectories of two point vortices near rectilinear topography can be determined explicitly[10] in terms of conserved quantities: the circulation, Γ, energy $\mathcal{E}$, and impulse, $\mathcal{I}$. For circular topography, the linear impulse $\mathcal{I}$ is replaced by the angular impulse

$$\mathcal{J} = \sum_j \Gamma_j H_j r_j^2. \tag{25}$$

In terms of the new variables $\lambda = \frac{1}{2}(r_1 + r_2)$ and $\phi = \theta_1 - \theta_2$, the radial distance of vortex pairs $r_{1,2}$ can be written as

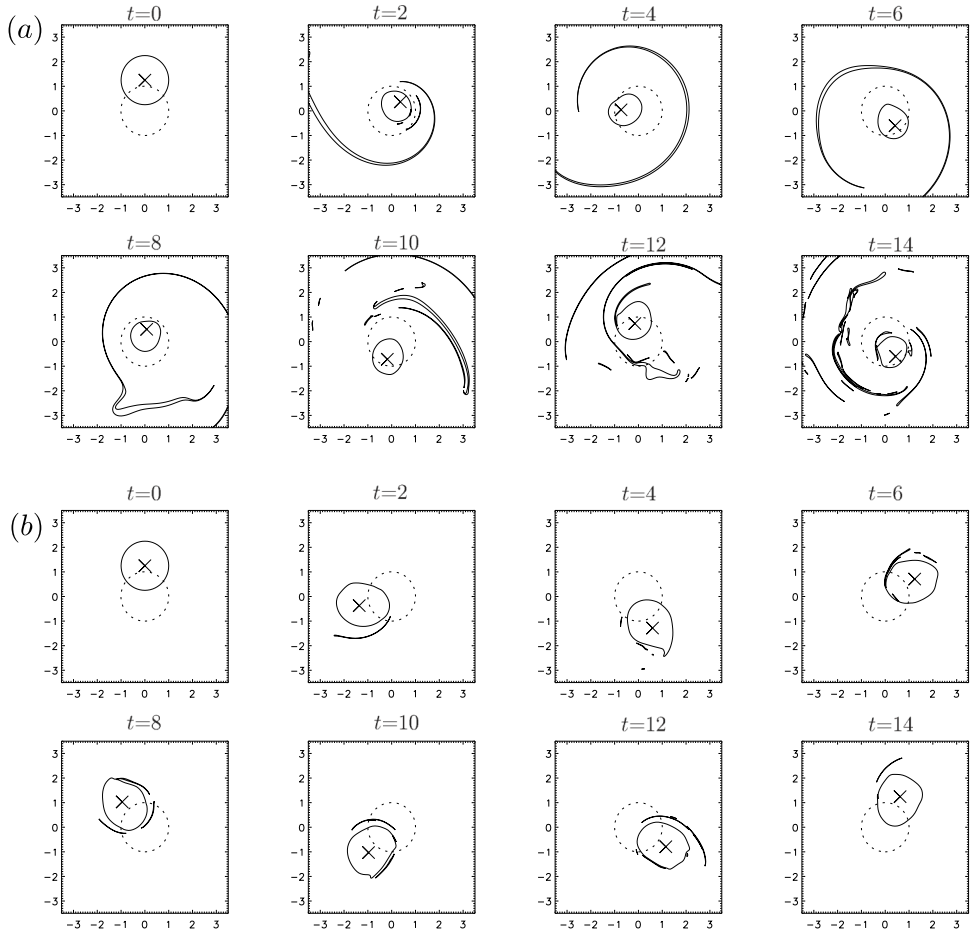

FIG. 8. The evolution of an initially circular vortex. Frames are at equal time intervals up to 10 turnover times. The initial configurations differ only in the depth ratio. (a) $\gamma = 3$. (b) $\gamma = 2$.

$$r_1 = \lambda + \frac{\mathcal{J}}{2H^+\lambda\Gamma}, \qquad r_2 = \lambda - \frac{\mathcal{J}}{2H^+\lambda\Gamma}. \tag{26}$$

Trajectories for the vortices follow from contours of the Hamiltonian, (24), in (λ, ϕ)-space. Since a point vortex cannot cross the step, λ cannot decrease below the minimum value

$$\lambda_{min} = \frac{1}{2}\left(1 + \sqrt{1 + \frac{2\mathcal{J}}{\Gamma H^+}}\right), \tag{27}$$

corresponding to when one vortex of the pair approaches the topography. This lower bound is plotted in Figures 9 and 10 with a bold line, and the forbidden area, $\lambda < \lambda_{min}$, hatched.

1. A point-vortex pair approaching a seamount, $\gamma < 1$

Trajectories for a point-vortex pair approaching a seamount with $\gamma = 1/2$ are given in Fig. 9 and can be divided into four different families. Figure 9(i) shows a typical trajectory in the line-shaded region of (λ, ϕ)-space: as a pair initially far from the seamount (i.e., $\lambda \gg 1$) approaches the seamount, the partial images (of opposite sign) slow the vortices, scattering them so that both vortices pass on the same side of the seamount (i.e., the trajectory in (λ, ϕ)-space passes through $\phi = 0$), before eventually propagating away.

In the unshaded region of (λ, ϕ)-space, the trajectories are again open so trajectories in (x, y)-space are aperiodic. The vortex pair approaches the seamount and is slowed by the partial images

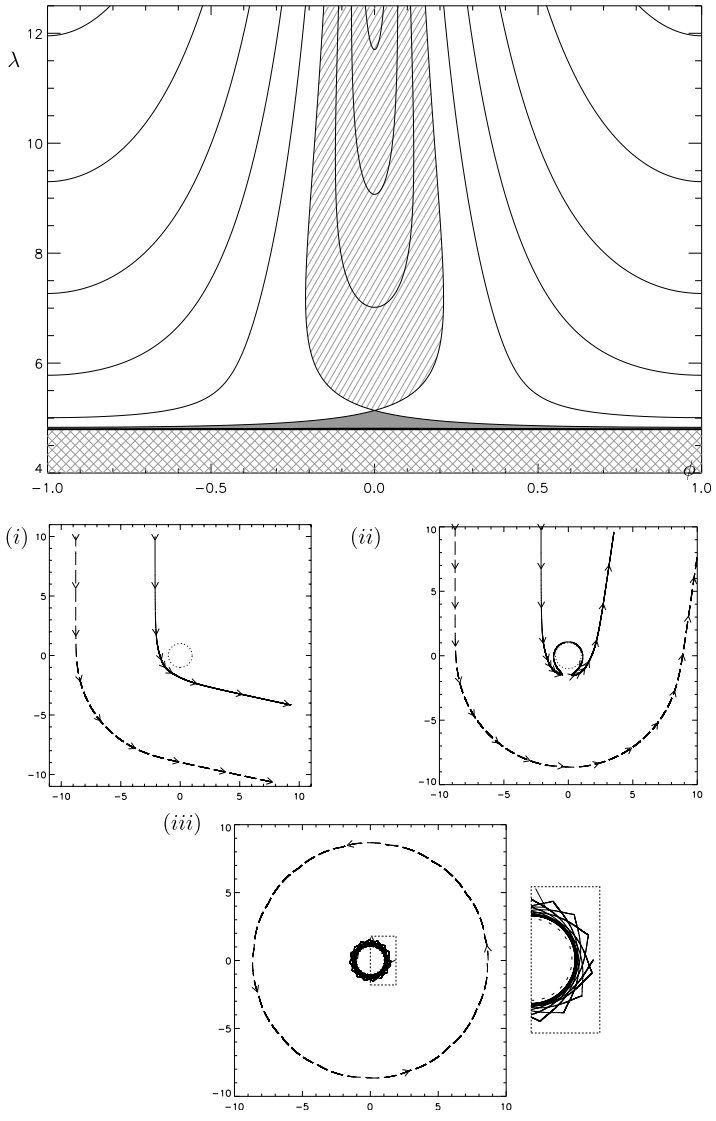

FIG. 9. Trajectories of point vortices exterior to circular seamount with $\gamma = 1/2$ and $\mathcal{J} \approx 228$. Shadings in (λ, ϕ)-space show the different families of trajectories with examples of each type of trajectory in (x, y)-space given by (i) line-shaded, (ii) unshaded, and (iii) solid-shaded. The dotted box shows an exploded view of the trajectory of the inner vortex in (iii), with the escarpment dashed. The cross hatched area, here and subsequently, shows the forbidden area where $\lambda < \lambda_{min}$. The arrow heads are drawn at equal time intervals.

but now the vortex closest to the seamount pairs with its partial image and propagates rapidly around the seamount leaving its partnering vortex to translate more slowly around the topography as in Figure 9(ii). The pair splits and the constituent vortices pass on opposite sides of the seamount. In (λ, ϕ)-space, the trajectory passes through $\phi = \pi$. Soon after, the vortex closer to the seamount is advected away from the seamount by the other more slowly translating vortex. The vortices then pair up again and translate away from the seamount with the resulting trajectory in (x, y)-space being scattered significantly by the topography.

Since (λ, ϕ)-space is periodic in the ϕ direction, trajectories in the solid-shaded region of (λ, ϕ)-space trajectories are closed. This corresponds to periodic motion in (x, y)-space, where vortices are trapped, circling the seamount in opposite directions. Therefore, when the pair interact strongly with each other (i.e., when $\phi \approx 0$), the distant vortex advects the closer vortex away from the seamount. But the vortex closer to the seamount is translating more quickly and overtakes

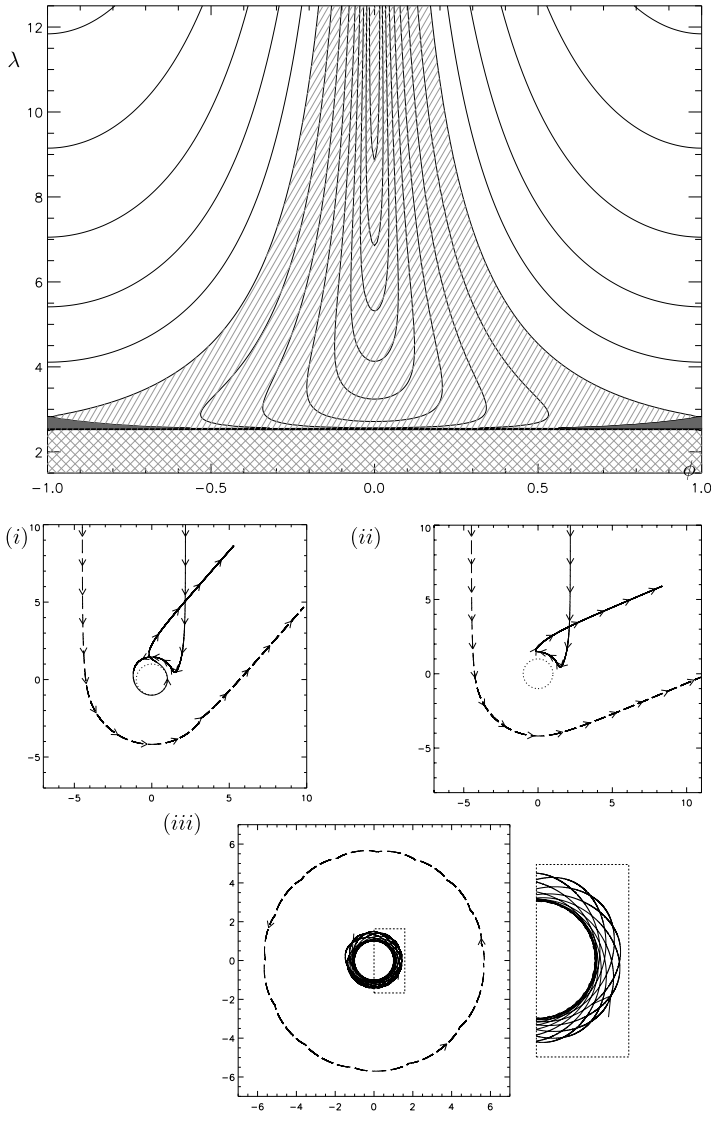

FIG. 10. As for Figure 9 but for trajectories exterior to circular well with $\gamma = 2$ and $\mathcal{J} \approx 12.1$.

the more distant vortex, such that the closer vortex is now advected back toward the seamount. The pair describes small-amplitude, leap-frogging motion as in the exploded view of Figure 9(iii). Similar leap-frogging motion with rapid changes of direction has been observed for vortices near a rectilinear step.[10]

The last class of trajectories is represented by the hyperbolic point in (λ, ϕ)-space. This point represents a two-vortex equilibrium state where both vortices are in steady rotation around the seamount with $\phi = 0$ such that they rotate on the same side of the topography. These states can be computed straightforwardly for both point vortices and vortex patches but being associated with a hyperbolic point they can be expected to be unstable and integrations for patches (not shown here) show that this is indeed the case.

2. A point-vortex pair approaching a well, $\gamma > 1$

A vortex outside circular topography with $\gamma > 1$ (i.e., a well) experiences a topographic image of the same-sign as the vortex. This is particularly significant for a pair with $\mathcal{J} = 0$ which approaches the well head-on. If the inter-vortex separation far from the well is sufficiently large,

the constituent vortices pass on either side of the well. However, if the separation is small then the pair does not pass the well. The constituent vortices pair with their respective images and propagate around the topography in opposite directions, eventually colliding at a point on the boundary of the well. There is thus a critical far-field vortex separation below which the constituent vortices will collide at the well boundary. This value can be found by setting $r_1 = r_2 = \rho$ and $\phi = \pi$, corresponding to a head-on collision form large distance, in (24) so

$$\mathcal{E}|_{\phi=\pi} = 4\rho^2\left(\frac{\rho^2+1}{\rho^2-1}\right)^{2\alpha}. \tag{28}$$

The minimum value of (28) occurs when constituent vortices only just avoid colliding with each other, and gives the minimum separation

$$\rho = \sqrt{2\alpha + \sqrt{4\alpha^2+1}}. \tag{29}$$

Using (24), the energy for this trajectory, known henceforth as $\mathcal{E}_s$, can be computed thereby giving a minimum value of energy below which the pair collides with the topography. In (λ,ϕ)-space, this leads to trajectories in $\lambda < \lambda_{min}$.

Figure 10 shows trajectories for a vortex pair near a well with $\gamma = 2$ in (λ,ϕ)-space with example trajectories in (x,y)-space. Similarly to the previous case where $\gamma < 1$, trajectories of a point-vortex pair fall into four distinct families, although the behaviour in each regime is subtly different. Consider first, as it is simpler, the unshaded region in Figure 10, with typical (x,y)-space trajectory given in Figure 10(ii). Here a distant point-vortex pair approaches the well. Near the well each vortex experiences an image of the same-sign circulation. The vortex nearer the well slows and "pairs-off" with its image and starts translating around the well, as does its partner, albeit at a slower rate (as it is further from the well). After the pair has passed through $\phi = \pi$, the vortex closest to the well moves away from the well as it re-pairs with the distant vortex. The pair then translate away from the topography so that eventually $\lambda \gg 1$.

The second class of trajectory is associated with the line-shaded region of Figure 10, with a typical trajectory given by Figure 10(i). As for the unshaded region, an initially distant pair approaches the well and is attracted by partial images of the same-sign. However in this case, the vortex closest to the topography becomes almost trapped by the well such that in (λ,ϕ)-space the trajectory passes through $\phi = 0$. After this vortex makes one complete orbit in (x,y)-space it re-pairs with the other, more distant vortex and the pair translate away from the well.

The third class of trajectory occurs when the pair is trapped by the well, given by the solid-shaded region in Figure 10. Here the vortices orbit the well at different angular speeds. However, in contrast to the case $\gamma < 1$, the pair orbits in the same direction. Therefore, when the vortices interact with each other strongly, the closer vortex is forced toward the well and no leap-frogging motion occurs. A typical trajectory (with an exploded view) is given in (x,y)-space by Figure 10(iii).

The last class of trajectories, as in Section V B 1, is located the at hyperbolic point in (λ,ϕ)-space which divides the trajectories described above. This point gives a two-vortex equilibrium state where both vortices are motionless, held stationary with $\phi = \pi$ on opposite sides of the topography by their images.

C. Vortex-patch trajectories

As for rectilinear topography, many of the properties of vortex-patch trajectories follow from the above classification of point-vortex trajectories although, since vortex patches can cross the topographic step, trajectories impinging on the topography can differ significantly from point-vortex trajectories and so are noted briefly here.

The evolution of a vortex-patch pair consisting of two finite-area, equal-volume, patches of oppositely signed uniform vorticity is found using an adaptation of the contour dynamics algorithm. Two cases are examined: first, when the pair translates towards a seamount with $\gamma = 1/2$ and second, when the pair translates towards a well with $\gamma = 2$. The patches are initialized far from the topography so that initially topographic effects are small. Further, each patch is centred around a

point-vortex trajectory that has the energy and impulse of the trajectory that follows the separatrix in (λ, ϕ)-space, so the most interesting patch trajectories can be observed. In all computations, the topography has unit radius and the initial separation of the pair is approximately 6.66 with each patch having area $\pi/2$. Each patch is discretized into 128 nodes around its boundary and is subjected to a loss of volume of less than 1% during the simulation unless stated otherwise.

1. A vortex-patch pair approaching a seamount, $\gamma < 1$

Figure 11 shows three examples of vortex-patch centroid trajectories with $\gamma = 1/2$ in both (x, y)-space and also (λ, ϕ)-space, where an equivalent (in terms of energy and impulse) point-vortex pair trajectory is included for comparison. Here and in Sec. V C 2, the patch pairs are initialized to have energies, $\mathcal{E}$, equal to $0.99\mathcal{E}_s$, $\mathcal{E}_s$, and $1.01\mathcal{E}_s$ where $\mathcal{E}_s$ is the energy of the point-vortex pair that passes through the separatrix. The agreement between the computed patch and an equivalent point-vortex trajectories is good. In Figure 11(a), where $\mathcal{E} < \mathcal{E}_s$, the patches remain close to circular and do not touch the seamount. Consequently, point-vortex and patch-pair trajectories are virtually identical. The agreement is still excellent in Figure 11(b), when $\mathcal{E} = \mathcal{E}_s$. Here the patch closest to the seamount just touches the topography before moving away from the seamount. Unlike its point vortex equivalent, the pair does not bifurcate. When the patch pairs are initialized with $\mathcal{E} > \mathcal{E}_s$, as in Figure 11(c), the patch pair trajectory deviates significantly from the point-vortex trajectory. One patch from the pair briefly straddles the seamount, allowing the trajectory to enter $\lambda < \lambda_{min}$, the region of parameter space not accessible to point vortices.

2. A vortex-patch pair approaching a well, $\gamma > 1$

Figure 12 shows the evolution of a vortex-patch pair translating toward a well with $\gamma = 2$. As in Section V C 1, the three energy levels $0.99\mathcal{E}_s$, $\mathcal{E}_s$, and $1.01\mathcal{E}_s$ are considered. In Figure 12(a), where $\mathcal{E} < \mathcal{E}_s$, the pair approaches the topography with each vortex attracted towards the well. One vortex straddles the well, propagating around the step and then moving wholly over the well before leaving under the influence of its partnering vortex. This path is close to that of the equivalent point-vortex motion except when the vortex patch straddles the well and the point-vortex approximation is inapplicable.[11] In Figure 12(b), where $\mathcal{E} = \mathcal{E}_s$, as in part (a), one vortex of the pair straddles the well. However, here the partnering vortex also propagates further around the well causing the straddling vortex to follow cycloid-like trajectories over the escarpment, shedding a small, but finite, amount of vorticity. Eventually, under the influence its partnering vortex, the straddling vortex breaks free of the well and moves away. In Figure 12(c), where $\mathcal{E} > \mathcal{E}_s$ the patch pair and point-vortex trajectories agree well. Here one vortex touches the well before translating away but does not straddle the topography. As in Figure 8(a), computations for larger changes in depth (not shown) show that straddling vortices can breakup.

VI. DISCUSSION

A novel approach for computing the velocity field using contour dynamics, avoiding extra computations or modifications to the Green's function is presented and used to find V-states and to examine the evolution of a vortex-patch pair close to circular topography of arbitrary height. Finite-area monopolar V-states for circular topography in shallow water are "tear" shaped with the vortex stretched towards the topographic boundary by an attracting image in deep water. V-states in deep water flatten along the side closest to the topography, with flattening becoming more pronounced as the V-state approaches the escarpment in the same way as in Euler equation V-states near walls.[12–14,16] The agreement in angular velocity between a computed V-state and an equivalent point vortex was found to be close provided the V-state remains close to circular. Importantly, unlike a point vortex, the angular velocity of a V-state is finite even when the V-state is straddling the topography.

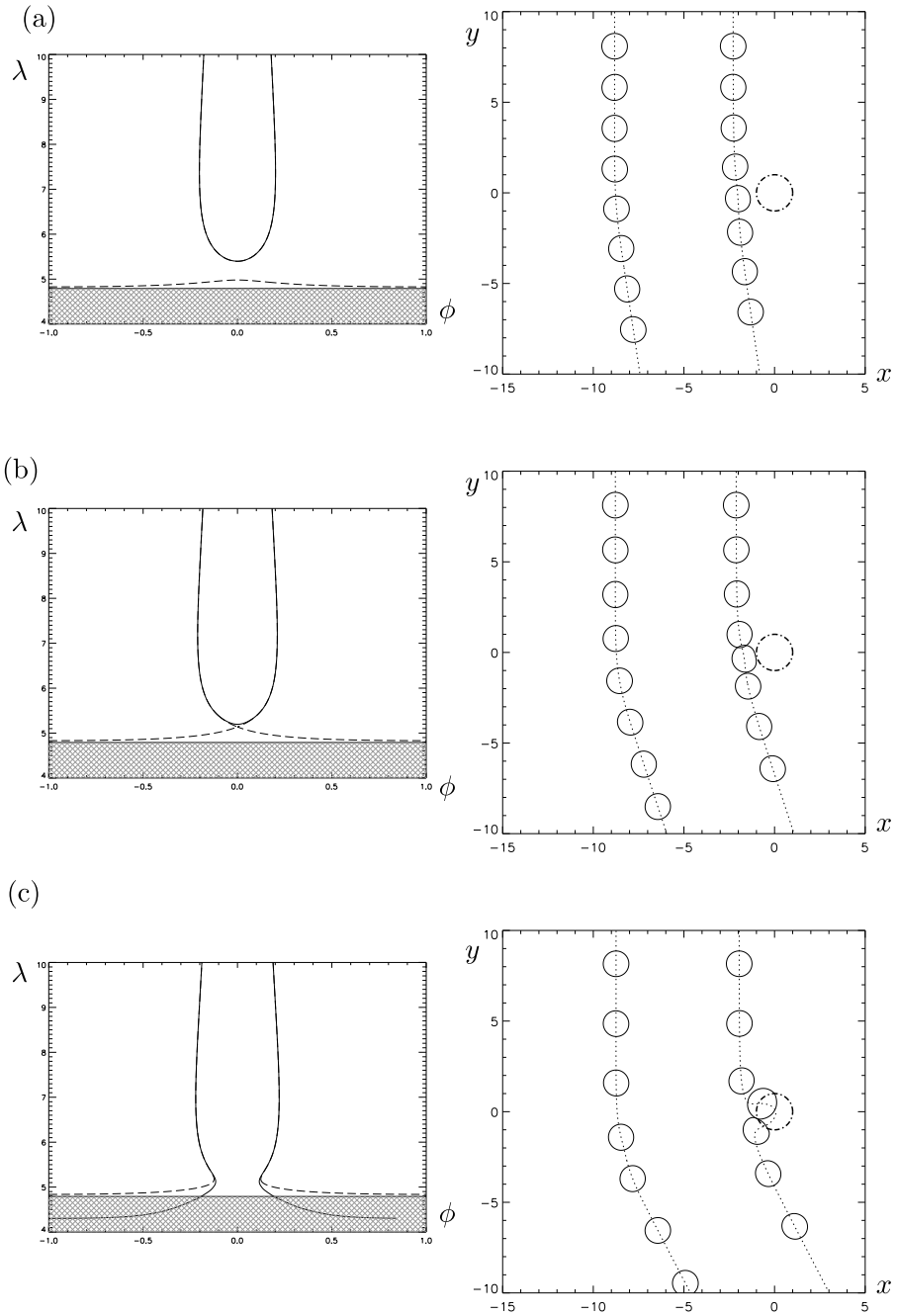

FIG. 11. Centroid trajectories for vortex-patch pairs approaching a seamount with $\gamma = 1/2$ for pairs of three different energies, $\mathcal{E}$. A pair with (a) $\mathcal{E} = 0.99\mathcal{E}_s$, (b) $\mathcal{E} = \mathcal{E}_s$, (c) $\mathcal{E} = 1.01\mathcal{E}_s$. Each part shows the centroid trajectory in (λ, ϕ)-space (solid line) and in (x, y)-space (dotted line). The (x, y) plot includes snapshots of the patches at equal time intervals, with the escarpment shown as a bold dashed-dotted circle. The (λ, ϕ) plot includes the trajectory of the equivalent point-vortex pair as a dashed line, obscured for the most part by the solid trajectory of the patch pair. The point-vortex forbidden region, where $\lambda < \lambda_{min}$, is hatched.

Time-dependent flows initialized with a V-state showed little change in vortex shape even after 25 turnover times, showing that V-states are robust, stable structures. Further, time-dependent flows starting with circular patches suggest that V-states act as attractors provided that a vortex is able to efficiently shed vorticity. It was found that non-straddling patches do not approach a V-state since there is minimal shedding. If depth changes are too large, as in Figure 8, the vortex does not

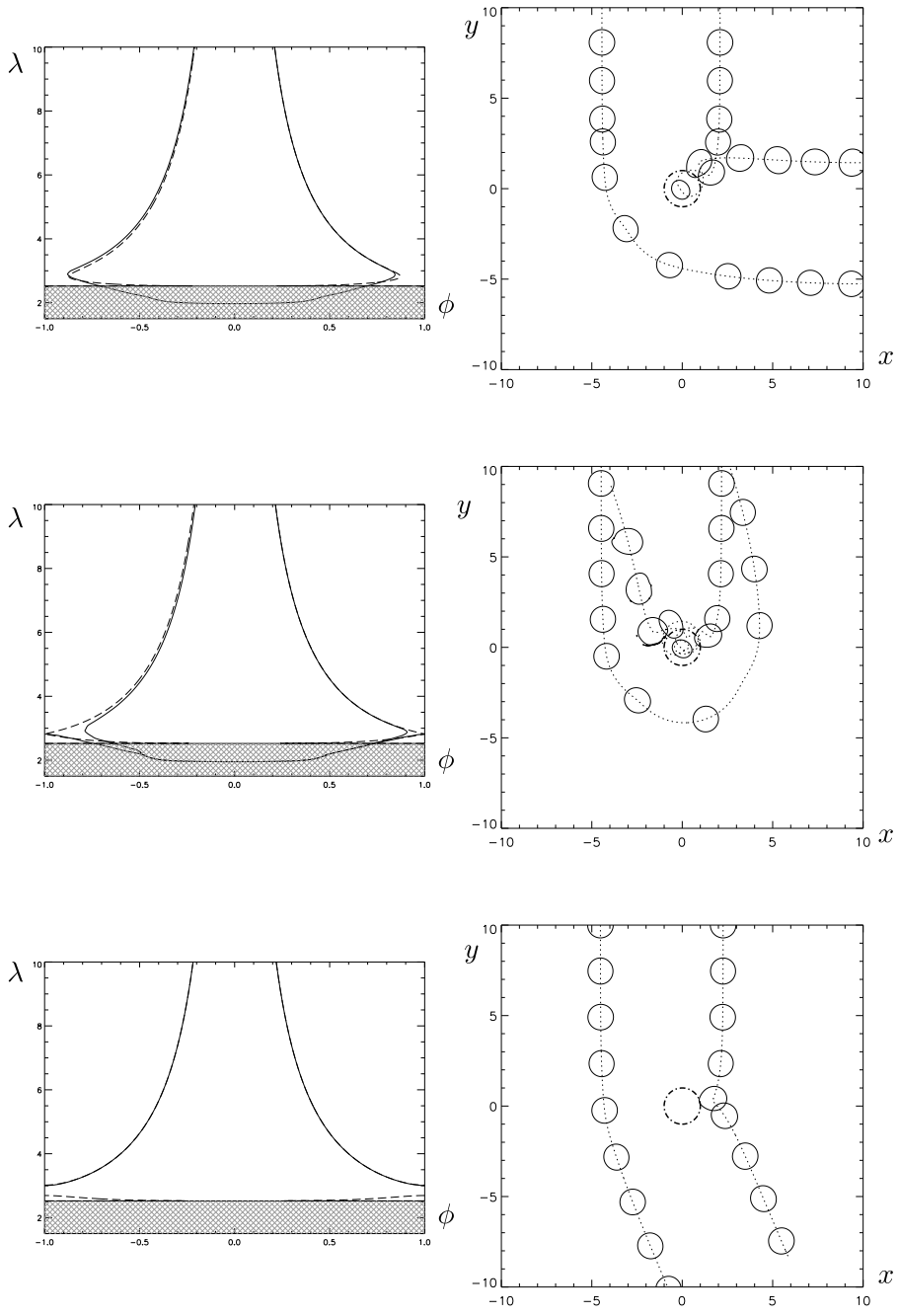

FIG. 12. As for Figure 11 but for a vortex-patch pair approaching a well with $\gamma = 2$.

remain coherent. The combination of these properties means that V-states are likely to be important transport mechanisms around small islands and wells with their ability to capture and transport anomalous fluid.

The behaviour of a point-vortex pair exterior to finite-height circular topography was described including the limiting cases of surface-piercing topography (an island) and a deep well. The trajectories of point-vortex pairs were obtained explicitly from their Hamiltonian. Point-vortex trajectories which approach the topography can be classified into four distinct categories: first when both vortices of a pair pass on the same side of the topography, second when the pair splits as it approaches the topography and vortices pass on opposite sides, third when the pair is trapped by

the topography with each vortex in the pair having different orbital frequency, and finally a steady configuration where for $\gamma > 1$ each vortex comprising the pair orbits with identical frequency, or for $\gamma < 1$ each vortex is held stationary by the topography. Vortex-patch trajectories were computed using contour dynamics and comparisons were made with point-vortex trajectories. Provided the patches remained close to circular during their evolution, vortex-patch trajectories compared well with point-vortex trajectories. Comparisons were less accurate when a patch straddled the topography.

The results above have been derived for purely inviscid flow. In addition to the rupturing effects over extreme escarpments noted here, viscosity and turbulence, particularly in shallow coastal flows, can act to limit the lifetime of coherent structures, although even in laboratory experiments with strong viscous dissipation vortices can be sufficiently long lived to interact with topography.[28] Near boundaries the no-slip viscous boundary condition means that vortices induce oppositely signed vorticity in a layer at the wall. Provided the flow is smooth and the Reynolds number is high, vortical fluid remains in the boundary layer and does not affect the fluid motion. At separation points, and particularly at sharply changing boundaries, vortical fluid can be ejected into the interior of the fluid domain and alter the interior dynamics. These effects can be incorporated into an inviscid framework[29] giving a simple but realistic oceanographic model.[30]

ACKNOWLEDGMENTS

A.K.H. acknowledges financial support from a UK Engineering and Physical Sciences Research Council graduate training award.

APPENDIX A: THE VELOCITY NEAR THE ORIGIN

When $|z|, |z_0| < 1$, expression (21) has two singularities of equal and opposite strength at $z = 0$. This section notes an alternative formulation that is valid and accurate for all $|z|, |z_0| < 1$. The image term in (18) can be expanded as

$$\frac{\alpha H^-}{2\pi} \log|1 - z\bar{z}_0| = \frac{\alpha H^-}{2\pi} \mathrm{Re} \sum_1^\infty \frac{(z\bar{z}_0)^n}{n}. \tag{A1}$$

Differentiating with respect to z and taking the complex conjugate gives the associated complex velocity

$$u + \mathrm{i}v = \frac{\alpha H^-}{2\pi} \sum_1^\infty \bar{z}^{n-1} \iint_{\mathcal{A}} z_0^n \, \mathrm{d}x_0 \, \mathrm{d}y_0 = \frac{\alpha H^-}{2\pi} \sum_1^\infty \frac{\bar{z}^{n-1}}{n+1} \oint_{\partial\mathcal{A}} z_0^{n+1} \, \mathrm{d}y_0, \tag{A2}$$

where the final reduction is through Green's theorem on noting that $\partial z_0^{n+1}/\partial x_0 = (n+1)z_0^n$. Now

$$\oint_{\partial\mathcal{A}} z_0^{n+1} \, \mathrm{d}z_0 = 0, \tag{A3}$$

as the integrand is entire. Combining real and imaginary parts of (A2) and (A3) gives a power series expansion for the image-induced velocity near $z = 0$,

$$u - \mathrm{i}v = -\frac{\mathrm{i}\alpha H^-}{4\pi} \sum_1^\infty \frac{z^{n-1}}{n+1} \oint_{\partial\mathcal{A}} \bar{z}_0^{\,n+1} dz_0. \tag{A4}$$

APPENDIX B: V-STATES NEAR CIRCULAR TOPOGRAPHY

Steady vortex patches rotating with constant angular velocity about an arbitrary point can be found efficiently by using a combination of contour dynamics to compute the velocity field and an algorithm which adjusts the contour toward a state such that the boundary is tangential to the

local velocity.[14] Vortex patches that rotate with constant angular velocity about their centroid have already been found.[14] Since the vortex patches studied here rotate about a point other than the centroid of the patch itself the algorithm must be modified accordingly. Essentially, if the vortex patch was to rotate with angular velocity Ω, then the boundary would remain invariant in a background solid body rotation with speed Ω. Therefore on the boundary of the vortex patch

$$\Psi(r,\theta) + \frac{\Omega}{2} r^2(\theta) = c, \tag{B1}$$

where Ψ is the streamfunction of the vortex induced flow and (r,θ) are polar coordinates from the centre of the topography (and here the centre of rotation) to the boundary of the vortex. After differentiating (B1), discretizing with $N+1$ nodes yields

$$u_{k+1/2}\Delta y_k - v_{k+1/2}\Delta x_k + (\Omega/2)\Delta(r_k^2) = 0, \qquad 1 \le k \le N, \tag{B2}$$

where the subscript $k+1/2$ denotes the mean value of the quantity between nodes k and $k+1$, i.e., $u_{k+1/2} = (u_k + u_{k+1})/2$ and $\Delta y_k = y_{k+1} - y_k$. It is possible to find Ω at each iteration by computing the velocity at each node and summing (B2) over the N nodes.

To iterate the vortex boundary closer to a V-state, choose polar coordinates $(R(\Theta),\Theta)$ centred at an appropriate point, $(\tilde{x},\tilde{y})$ such that $R(\Theta)$ remains single valued for $0 \le \Theta \le \pi$ (possible as every V-state has a line of symmetry). Then (B2) can be written as

$$r_k - f_{k+1/2} r_{k+1} = 0, \quad 1 \le k \le N, \quad \text{or,} \quad r_k - f_{k-1/2}^{-1} r_{k-1} = 0, \quad 2 \le k \le N+1, \tag{B3}$$

where $f_{k+1/2}$ is defined as

$$f_{k+1/2} \equiv \frac{u_{k+1/2}\sin\Theta_{k+1} - v_{k+1/2}\cos\Theta_{k+1} + \Omega(2R_{k+1} + \tilde{y}\sin\Theta_{k+1} + \tilde{x}\cos\Theta_{k+1})}{u_{k+1/2}\sin\Theta_k - v_{k+1/2}\cos\Theta_k + \Omega(2R_k + \tilde{y}\sin\Theta_k + \tilde{x}\cos\Theta_k)}, \tag{B4}$$

this reduces to the form of the translating vortex near a wall when $\sqrt{\tilde{x}^2+\tilde{y}^2} \to \infty$ and the rotating vortex when $\sqrt{\tilde{x}^2+\tilde{y}^2} \to 0$.[14] It is straightforward to arrange (B3) into a tri-diagonal system and solve for $R_k, k = 1,\ldots,N+1$.

[1] P. L. Richardson and A. Tychensky, "Meddy trajectories in the Canary Basin measured during the SEMAPHORE experiment, 1993-1995," J. Geophys. Res. **103**, 25029–25045, doi:10.1029/97JC02579 (1998).
[2] D. Fratantoni, W. Johns, and T. Townsend, "Rings of the North Brazil Current: Their structure and behaviour inferred from observations and numerical simulation," J. Geophys. Res. **100**, 10633–10654, doi:10.1029/95JC00925 (1995).
[3] D. H. Peregrine, "Surf zone currents," Theor. Comput. Fluid Dyn. **10**, 295–309 (1998).
[4] K. A. Gorshkov, L. A. Ostrovsky, and I. A. Soustova, "Perturbation theory for Rankine vortices," J. Fluid Mech. **404**, 1–25 (2000).
[5] P. Orlandi, "Vortex dipoles impinging on circular cylinders," Phys. Fluids A **5**, 2196–2206 (1993).
[6] R. Verzicco, J. B. Flor, G. J. F. van Heijst, and P. Orlandi, "Numerical and experimental-study of the interaction between a vortex dipole and a circular-cylinder," Exp. Fluids **18**, 153–163 (1995).
[7] E. R. Johnson and N. R. McDonald, "The motion of a vortex near two circular cylinders," Proc. R. Soc. A **460**, 939–954 (2004).
[8] D. G. Crowdy and J. S. Marshall, "The motion of a point vortex around multiple circular islands," Phys. Fluids **17**, 056602 (2005).
[9] E. R. Johnson and N. R. McDonald, "Surf-zone vortices over stepped topography," J. Fluid Mech. **511**, 265–283 (2004).
[10] A. K. Hinds, E. R. Johnson, and N. R. McDonald, "Interactions of two vortices near step topography," Phys. Fluids **19**, 126602 (2007).
[11] E. R. Johnson, A. K. Hinds, and N. R. McDonald, "Steadily translating vortices near step topography," Phys. Fluids **17**, 056601 (2005).
[12] G. S. Deem and N. J. Zabusky, "Vortex waves: Stationary 'V-states,' interactions, recurrence, and breaking," Phys. Rev. Lett. **40**, 859–862 (1978).
[13] R. T. Pierrehumbert, "A family of steady, translating vortex pairs with distributed vorticity," J. Fluid Mech. **99**, 129–144 (1980).
[14] H. M. Wu, E. Overman, and N. J. Zabusky, "Steady state solutions of the Euler equations in two-dimensions. Rotating and translating V-states with limiting cases. I. Numerical algorithms and results," J. Comput. Phys. **53**, 42–71 (1984).
[15] D. G. Dritschel, "A general theory for two-dimensional vortex interactions," J. Fluid Mech. **293**, 269–303 (1995).
[16] P. G. Saffman and S. Tanveer, "The touching pair of equal and opposite uniform vortices," Phys. Fluids **25**, 1929–1930 (1982).
[17] E. R. Johnson and N. R. McDonald, "The motion of a vortex near a gap in a wall," Phys. Fluids **16**, 462–469 (2004).
[18] E. R. Johnson and N. R. McDonald, "Vortices near barriers with multiple gaps," J. Fluid Mech. **531**, 335–358 (2005).
[19] E. R. Johnson and S. R. Clarke, *Numerical Methods for Fluid Dynamics* (Oxford University Press, 1998), Vol. 7.

[20] P. H. Haynes, E. R. Johnson, and R. G. Hurst, "A simple model of Rossby-wave hydraulic behavior," J. Fluid Mech. **253**, 359–384 (1993).
[21] D. Crowdy and A. Surana, "Contour dynamics in complex domains," J. Fluid Mech. **593**, 235–254 (2007).
[22] P. G. Saffman, *Vortex Dynamics* (Cambridge University Press, 1992).
[23] E. R. Johnson, "Trapped vortices in rotating flow," J. Fluid Mech. **86**, 209–224 (1978).
[24] L. M. Milne-Thomson, *Theoretical Hydrodynamics* (Macmillan, New York, 1955).
[25] D. G. Dritschel, "Contour surgery: A topological reconnection scheme for extended integrations using contour dynamics," J. Comput. Phys. **77**, 240–266 (1988).
[26] O. Bühler and T. E. Jacobson, "Wave-driven currents and vortex dynamics on barred beaches," J. Fluid Mech. **449**, 313–339 (2001).
[27] M. E. Stern, "Scattering of an eddy advected by a current towards a topographic obstacle," J. Fluid Mech. **402**, 211–223 (2000).
[28] A. K. Hinds, I. Eames, E. R. Johnson, and N. R. McDonald, "Laboratory study of vortex dipoles interacting with step topography," J. Geophys. Res. **114**, C06006, doi:10.1029/2008JC005210 (2009).
[29] O. R. Southwick, E. R. Johnson, and N. R. McDonald, "A point vortex model for the formation of ocean eddies by flow separation," Phys. Fluids **27**, 016604 (2015).
[30] O. R. Southwick, E. R. Johnson, and N. R. McDonald, "A simple model for sheddies: Ocean eddies formed from shed vorticity," J. Phys. Oceanogr. **46**, 2961–2979 (2016).